A learnt approach for the design of magnetically actuated shape forming soft tentacle robots

Peter Lloyd[1], Ali Kafash Hoshiar[2], Tomas da Veiga[1], Aleks Attanasio[1], Nils Marahrens[1], James H. Chandler[1] and Pietro Valdastri[1]

***Abstract*—Soft continuum robots have the potential to revolutionize minimally invasive surgery. The challenges for such robots are ubiquitous; functioning within sensitive, unstructured and convoluted environments which are inconsistent between patients. As such, there exists an open design problem for robots of this genre. Research currently exists relating to the design considerations of on-board actuated soft robots such as fluid and tendon driven manipulators. Magnetically reactive robots, however, exhibit off-board actuation and consequently demonstrate far greater potential for miniaturization and dexterity. In this paper we present a soft, magnetically actuated, slender, shape forming 'tentacle-like' robot. To overcome the associated design challenges we also propose a novel design methodology based on a Neural Network trained using Finite Element Simulations. We demonstrate how our design approach generates static, two-dimensional tentacle profiles under homogeneous actuation based on predefined, desired deformations. To demonstrate our learnt approach, we fabricate and actuate candidate tentacles of 2mm diameter and 42mm length producing *shape* profiles within 8% mean absolute percentage error of desired shapes. With this proof of concept, we make the first step towards showing how tentacles with bespoke magnetic profiles may be designed and manufactured to suit specific anatomical constraints.**

***Index Terms*—Modeling, Control, and Learning for Soft Robots; Soft Robot Materials and Design; Surgical Robotics: Steerable Catheters/Needles.**

I. Introduction

CONTINUUM Manipulators (CMs) have been used to assist with and enable surgical procedures in the form of catheters and endoscopes for at least the last 120 years [1]. Traditional CMs rely on body rigidity to transmit forces and torques from proximal to distal ends. This approach relies on operator skill, offers limited accuracy or dexterity and the process itself can cause tissue trauma [2]. These limitations may be mitigated with the use of soft robotic manipulators which are primarily fabricated from elastomeric materials and actuated through a wide range of methods as detailed in [3]. Common methods of actuation are fluid driven [4], tendon driven [5], shape memory alloy [6], electroactive polymer [7] and magnetic [8] systems. For the non-magnetic 'on-board' actuated systems a fundamental trade-off will always exist between dexterity and miniaturisation potential; for each additional degree of freedom (DoF) controlled within the manipulator, a further driveline (e.g. a fluid channel or tendon) must be added. This limitation does not apply to magnetic actuation and, consequentially, the magnetic approach exhibits far greater potential for miniaturisation and therefore surgical application than rival methods.

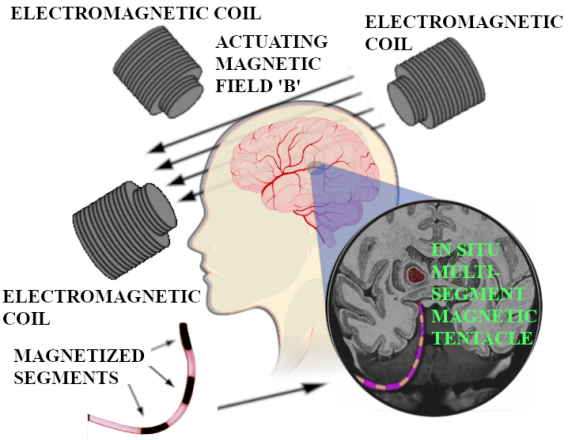

Figure 1. A sample application of the magnetically actuated tentacle – neurovascular catheter navigation. The target shape is derived from a pre-operative Magnetic Resonance Image of the brain. Under specific electromagnetic actuation, the desired shape is assumed.

Magnetically actuated tip driven systems [9] [10] have been demonstrated to increase control and reduce trauma [11], [12] during the negotiation of anatomical convolutions. Recently a number of works [13], [14], [8] have demonstrated the efficacy and miniaturisation potential of such catheters. These systems, however, can only assume the body shape of their respective conduit via anatomical interaction. A soft continuum robot equipped with full body-shape control would possess the potential to assume a predefined shape without relying on these forces. We would consider such a robot, with numerous wrenches acting along its length, to be 'fully shape forming' in contrast to the conventional tip driven manipulators. The magnetic shape control demonstrated in [15], [16] and [17] could, in principle, be exploited to provide a safe railroad to a predefined working location. This would

Manuscript received: October, 15, 2019; Revised February, 6, 2020; Accepted March, 5, 2020.

This paper was recommended for publication by Editor C. Laschi upon evaluation of the Associate Editor and Reviewers' comments. Research reported in this article was supported by the Royal Society, by the Engineering and Physical Sciences Research Council (EPSRC) under grant number EP/R045291/1, and by the European Research Council (ERC) under the European Union's Horizon 2020 research and innovation programme (grant agreement No 818045). Any opinions, findings and conclusions, or recommendations expressed in this article are those of the authors and do not necessarily reflect the views of the Royal Society, EPSRC, or the ERC.

[1] Peter Lloyd, Tomas da Veiga, Aleks Attanasio, Nils Marahrens, James H. Chandler and Pietro Valdastri are with the Storm Lab, School of Electronic and Electrical Engineering, University of Leeds, UK, {men9prl, eltgdv, elaat, elnma, J.H.Chandler, p.valdastri}@leeds.ac.uk

[2] Ali Kafash Hoshiar is with the School of Computer Science and Electronic Engineering, University of Essex, Colchester, UK, {a.kafashhoshiar@essex.ac.uk}

Digital Object Identifier (DOI): see top of this page.

enable improvements in safety, procedure time and patient comfort; this concept is shown schematically in Fig. 1. For real-world applications, the highly convoluted geometries and millimetre scale workspaces encountered make magnetic actuation a promising, if challenging, avenue of research. Magnetic actuation, however, comes with its own attendant complexities regarding the modelling and simulation of long, slender and therefore potentially unstable, magnetically active elastomers. Henceforth, we refer to our slender, shape forming, soft robots as magnetic tentacles.

Shape forming CMs presented in the literature exhibit a variety of modelling methods. Most prominently we observe the Cosserat rod [18], the constant curvature [19] and the rigid-link [20] models. Each model represents a level of approximation and attendant computational intensity deemed appropriate for its particular application. There also exists the set of magnetically actuated shape forming materials [21], [22], [16] which have heavily influenced this work. These tend to employ a full continuum mechanics model via commercial FEM packages as, generally, they are not considering closed loop control applications. The subset at the intersection of these two groups (where our work resides) is the magnetically actuated rectangular cross-section shape forming continuum robots appearing in [17] and [23]. These use a numerically intensive Fourier representation of manipulator shape to solve their statics and dynamics.

The concept of a fully flexible, shape forming tentacle robot fabricated from a magnetically active elastomer, orders of magnitude softer than present day catheters, represents a step change in the evolution of CM design. These tentacles can be pre-programmed to assume the profile of the conduit through which they are designed to pass. This relies on prior knowledge of the route in question - which may be derived from pre-operative imaging - and a methodology to translate this pathway into a magnetization profile. The contribution presented here offers a first step towards this goal coupled with a design methodology to overcome the inherent complications of magnetically active elastomers.

The two discrete functions of the tentacle can be defined as; quasi-static shape forming and dynamic shape forming. The first, quasi-static role, is to stiffen into a pre-defined shape upon arrival at a specific location such as the tumour at the base of the skull illustrated in Fig. 1. This stiffening would provide a safe and robust working channel for the delivery of treatment and the evacuation of tissue whilst also permitting the increased force required for cutting or ablation. The second, dynamic role, would incorporate shape forming during navigation to that same working location and would be driven by an in-homogeneous and transient magnetic field. The work presented here considers the quasi-static case under a planar, homogeneous and time invariant actuating field.

The first contribution of this work is to present the fundamental concept, including the fabrication process, of our fully soft, shape forming tentacle robots. The second contribution is our learnt approach to the two-dimensional design of these tentacles, actuated in a time-invariant homogeneous field. We employ a Finite Element Model (FEM) as the source of training data for a fully connected Artificial Neural Network (ANN). The output of the trained ANN represents the solution to the inverse statics of our soft robot - when we refer to forward and inverse *statics*, we are referring to the soft serial robot equivalent of kinematics in conventional hard robotics. The difference being the requirement, for a soft robot, of forces to maintain static equilibrium. This solution in turn informs the design of our experimental prototypes. The results produced by the ANN are validated for three demonstrative shapes in both the underlying FEM and, after fabrication, in our experimental setup.

II. Design Approach

Machine learning techniques which are driven by real-world experimental data can minimise or even bypass modelling assumptions. To train such networks, learning via demonstration [24], or input from a randomized feed (sometimes referred to as motor babble) [25] offer valid methods. However, in the absence of high-volume, reliable sensory data and the ability to rapidly prototype test samples these real-world approaches are unfeasible. For our design methodology we therefore employ a FEM as the source of training data for a fully connected ANN.

Utilizing FEM to simulate the interaction between magnetic and mechanical forces has been successfully demonstrated in previous work [21] and been successfully applied to CMs [8]. In addition, the use of ANNs as surrogates of FEMs has also been reported; for example in [26] and [27] convolutional neural networks are used to fully recreate FE simulations of a liver and an arterial wall respectively. These works exhibit results evidencing the effectiveness of deep learning in this particular sphere of research. To the authors knowledge there are no examples in the literature of Neural Network replication of Finite Element Modelling for CMs under magnetic actuation or otherwise.

The approach taken to realise our FEM surrogate ANN is comprised of the following steps: (1) a simplified single segment FEM is used to set modelling assumptions based on correlation with experimental data; (2) the FEM is extended to a functional number of magnetized segments; (3) a large number of simulations are performed to create a database for training validation and testing of the ANN; (4) the ANN is trained; (5) the ANN generalises for predefined, novel tentacle shapes; and (6) these shapes are verified in the multi-segment FEM, fabricated, and experimentally evaluated under a homogeneous magnetic field.

III. Modelling Approach

A. Constitutive Model

For the purposes of this study, we assume the elastomer in consideration is homogeneous, isotropic and, for the range of strains experienced herein, incompressible. Assuming a quasi-static state and entirely elastic deformation, under the Lagrangian description in [28], the deformation gradient tensor F is the partial derivative of the deformed position with respect to the relaxed position.

For the case of a magnetic material, torque when placed wholly within a homogeneous magnetic field, may be defined

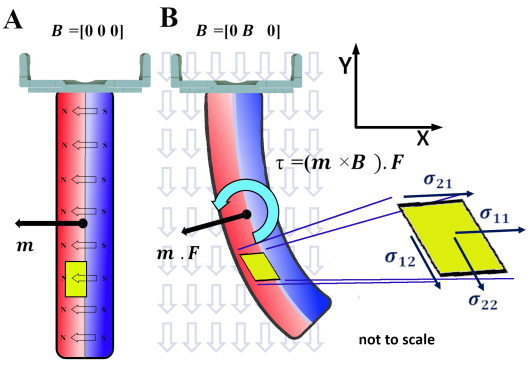

Figure 2. **(A)** The undeformed position under a zero actuating field, the tentacle is magnetized in the $-x$ direction. **(B)** The deformed position under an actuating torque τ generated by the field, B, applied orthogonally to the magnetization m. The deformation gradient tensor F influences the effective direction of magnetization. An exploded infinitesimal volume shows the Cauchy stress tensor σ in two dimensions.

as the cross product of magnetic moment (m) and the surrounding field of flux (B). This may be considered as the mechanical work of the magnetic torque performed to align the magnetic dipole moments [21]. Defining magnetization as $M = \frac{m}{V}$ we can say that the Cauchy stress tensor for magnetic effects is:

$$\sigma^{mag} = (M \times B) \cdot F \tag{1}$$

and with reference to the quasi-static assumption we can also state that, for the full Cauchy stress tensor:

$$div(\sigma) + f_g = 0 \tag{2}$$

where f_g is the body force vector per unit volume; equal to gravity as magnetic body forces are included in the stress tensor. These two equations can be solved for appropriate boundary conditions to give the deformation gradient tensor and thus the deflection of our tentacle due to magnetic actuation.

B. The Single Segment Cantilever Beam Model

Using the planar cantilever beam of uniform magnetization, depicted in Fig. 2, as our example, it is possible to compare experimental data with an analytic model and our FEM. This permits verification of our assumptions before we extend the FEM beyond the reach of any analytical solution. In the simple shear stress model, the symmetrical mechanical stress components net to zero leaving only the magnetic stress components contributing to bending moment. From Euler-Bernoulli beam theory we can thus say that:

$$\frac{\delta}{L} = \frac{(m_1 B_2) 16 L^2}{3 E d^2} \tag{3}$$

where δ is beam deflection, E is elastic modulus, L is length and d is diameter. As in [29], given invariant geometric and material properties, (3) offers a linear correlation between δ and B_2. To simulate the system, FEMs were constructed under the plane strain assumption in two dimensions in COMSOL multiphysics suite v5.4 (COMSOL AB, Stockholm, Sweden). The model employed solid mechanics and electromagnetics

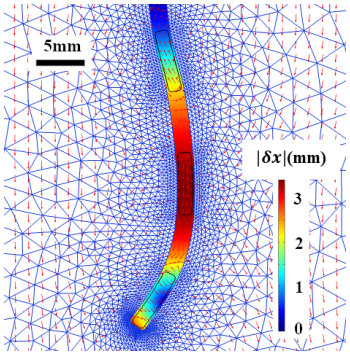

Figure 3. The multi-segment Finite Element Model: three discretely magnetized segments in a homogeneous background field. This is numerically represented by 238,000 spatially optimized nodes and produces a range of poses which are quantified by deflections in x and y at three Points of Interest down the length of the tentacle.

modules connected via the Maxwell surface stress tensor utilizing Newton-Raphson iterative convergence within the MUltifrontal Massively Parallel sparse direct Solver (MUMPS) option.

Due to the highly non-linear nature of the Maxwell equations, the mesh optimization process results in local mesh concentrations around the edges of the magnetized segments (visible in Fig. 3). These segment edges were constrained to 50 nodes per 7mm length and 25 nodes per 1.5mm diameter. A maximum element growth rate of 1.2 was applied throughout. The air domain in which the tentacle is suspended is 250mm x 250mm with a zero gradient boundary condition applied around its periphery. This domain has a maximum element growth rate of 1.1 and a maximum element size of 20mm. For the single segment cantilever case, the resultant model was comprised of 27,000 free triangular (two-dimensional) nodes.

C. The Multi-Segment Model

The multi-segment 'tentacle' structure was represented with three discrete segments of magnetically doped elastomer, 7.0mm long by 1.5mm diameter, embedded within the magnetically unreactive silicone, 42mm in length by 2mm in diameter. The magnetization direction of each segment can be independently controlled within the two-dimensional plane. To generate a geometrically accurate simulation, the resulting FEM, as shown in Fig. 3, was discretized using 238,000 free triangular (two-dimensional) nodes subject to the same constraints as the single segment mesh (Section III-B).

IV. THE ARTIFICIAL NEURAL NETWORK

The appeal of Machine Learning (ML) for our problem is its ability to generalize for previously unseen scenarios from sample data thus forecasting future outcomes in the absence of a constitutive model. This renders ML an ideal tool for solving contrived inverse static problems such as those occurring in hyper-redundant, elastomeric CMs.

A. The Dataset

In order to train an ANN, we need large quantities of data. In real world applications, as described previously, this can be produced via motor babble. To generate 'virtual motor babble',

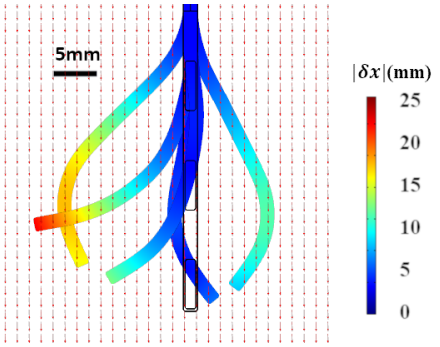

Figure 4. A visual sample of the 13,800 shapes generated during the 'virtual motor babble' phase. A snapshot of this process features in the supplementary video.

we parametrically swept each of the three magnetization input variables. For each magnetized segment of the tentacle the modulus of the magnetization vector remains unchanged, the only variable is the direction of magnetization. As such the input to be swept can be represented by three unit vectors representing magnetization direction.

An incremental rotation of the magnetization vector of $\frac{1}{24}$ of a revolution (24 possible values for each of 3 input variables) produces $24^3 = 13,824$ sequential entries. These actuating variables were fed as inputs to the pre-assembled FEM and run on a 3.2GHz, 32GB, 16 core Intel Xeon Gold processor in a total run time of 38 hours. This process generated a set of deflection vectors at each of three Points of Interest (PoI) corresponding to the magnetization vectors at those same PoI. To represent, as a point in space, the global position of a segment of non-zero volume, the centre of mass of each of the three magnetically active segments was chosen as the PoI. An example selection of resultant deformed tentacles is shown in Fig. 4.

As illustrated in Fig. 5, for each segment, the magnetization angle produces a deflection. This deflection reaches some maximum, beyond this point further increases in magnetization angle, θ, will begin to reduce deflection. This phenomenon produces a non-unique relationship between inputs and outputs – kinematic redundancy - something which is anathema to a Neural Network. It is therefore necessary to systematically

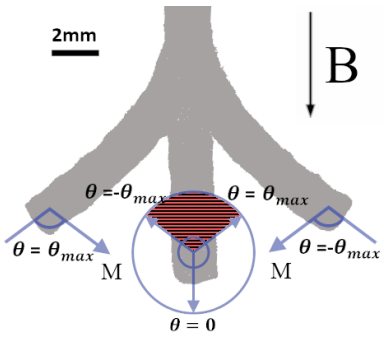

Figure 5. Schematic of the positive and negative angles of maximum deflection. For a fixed applied field 'B', and fixed initial pose a maximum deflection is achievable by applying a magnetization 'M' at an angle θ_{max}(or $-\theta_{max}$). The single segment tentacle is shown in grey with the unactuated pose in the centre of the image and the maximum and minimum deflections also shown. For magnetization angles greater than θ_{max} the resultant deflection will drop, rendering results produced by magnetizations in the red shaded region repetitious.

remove duplicate results; those vectors residing in the red shaded region of Fig. 5, from each of the three actuating segments. The resulting lookup table reduces from 13,824 systematically produced entries to 2298 unique solutions each with 6 dimensions of input data (two-dimensional magnetization vectors at three PoI) and a corresponding 6 dimensions of output data (two-dimensional deflection vectors at the same three PoI). These planar deflection vectors are simplified to scalars, representing the lateral x-displacement of the PoI on the actuated manipulator to the unactuated centreline. Under the assumption of negligible tentacle extension (under 5mT actuation a maximum stretch of 0.1% is observed in the numerical model) it can be assumed that y-deflection is purely a function of x-deflection i.e. only one DoF exists per segment. This dataset is split 70% for training, 15% for validation and 15% for testing.

B. The Learning Network

The architecture of the ANN employed to replicate the FEM is a fully connected neural network with an output regression layer. The effect of variations in number of neurons and number of hidden layers was assessed based on runtime and validation accuracy and the final arrangement emerged containing 6 hidden layers of 20 neurons each. After iterating for 60 epochs of Levenberg-Marquardt backpropagation of error employing sigmoid activation functions this arrangement gave a 6.3% mean absolute percentage error (MAPE) at the validation (inverse model) phase.

V. Fabrication

A. The Single Segment

The single segment was fabricated from Ecoflex 00-30 embedded with neodymium-iron-boron (NdFeB) microparticles with an average diameter of 5 μm (MQFP-B+, Magnequench GmbH, Germany). Particles of NdFeB were added to the prepolymer in a 1:1 ratio by weight equating to a volumetric ratio of 0.88:0.12 (Ecoflex:NdFeB). The composite was mixed and degassed in a high vacuum mixer (ARV-310, THINKYMIXER, Japan) at 1400 rpm, 20.0 kPa for 90 seconds and then injected onto a straight cylindrical mold of diameter d=1.5mm and length 20mm and left to cure. The mold contained a centrally aligned 0.25mm diameter Nitinol needle running for 10mm of its length. This needle remained embedded in the polymer and was used to suspend and constrain the specimen during testing. Once the polymer had cured, the specimen was subjected to a uniform field of 46.44 KGauss (4.644 T) (ASC IM-10-30, ASC Scientific, USA) orthogonal to the tentacle's principle axis.

B. The Multi-Segment Tentacle

For the multi-segment arrangement, the unmagnetized doped elastomer (Fig. 6A) was divided into three identical 7mm segments (Fig. 6B). Each segment was subsequently embedded, concentrically, at 14mm intervals (in the longitudinal direction) into an undoped silicone host (Ecoflex 00-30) (Fig. 6C). A centrally aligned 0.25mm Nitinol needle

supports the *full length* of the structure during fabrication. Upon curing this needle is removed save for the final 10mm which remains embedded to act as the mechanical constraint during experimentation. The total length of the multi-segment tentacle (Fig. 6D) is 52mm. From bottom to top this can be broken down as 10mm of constrained length followed by 42mm of unconstrained length. Undoped segments appear white and doped segments appear black. The dimensional accuracy of the fabricated tentacle samples was assessed through image analysis software (LAZ EZ, Leica, Germany), calibrated against a known reference length with images obtained using a digital light microscope (DMS300, Leica, Germany). Values of segment lengths (Mean+/-SD) were found to be 7.4+/-0.43mm, and segment diameters were 1.9+/-0.03mm. For future work it is planned that an automated fabrication technique would significantly reduce these errors and, for any systematic discrepancies, a post fabrication analysis could identify and incorporate these into simulations.

This arrangement was housed in a magnetizing tray (Fig. 6D) and exposed to the same 46.44 KGauss saturating field which was employed to magnetize the single segment. The geometry of the magnetizing tray was driven by the solution to the inverse static problem for the soft robot. This solution was generated by the Neural Network based on pre-defined desired deflections.

VI. Experimental Evaluation

A. The Single Segment

The single segment was hung vertically downwards on its embedded Nitinol needle in the centre of a Helmholtz coil (DXHC10-200, Dexing Magnet Tech. Co., Ltd, Xiamen, China). As in Fig. 7, 10mm of this 20mm section was constrained by the Nitinol needle and 10mm was free to deform. The Helmholtz coil was arranged so as to produce a vertically aligned homogeneous magnetic field. The current through the coils was ramped from -10mT to 10mT in 2mT increments to produce a piece-wise increasing actuating field orthogonal to the undeformed magnetization of the test piece. Images of the specimen were taken on a Nikon D5500 DSLR with an AF-S NIKKOR 18-55mm lens at each field strength and were post-processed in GIMP 2.10 prior to analysis. The maximum deflection was measured at the centre of the distal end of the specimen in both the numerical and experimental analyses. The experiment was repeated three times, the first iteration of which is shown in Fig. 7 and also in the supporting video.

This analysis was performed to verify the mechanical and magnetic properties of the doped elastomer. The Elastic modulus of the doped and undoped silicone was measured to be 91 kPa and 69 kPa respectively. These values were obtained using a uniaxial load tester (MultiTest 2.5-xt, Mecmesin, UK) operating up to a maximum of 100% strain. The Poisson's ratio was set to 0.5 for both elastomers representing the assumption of incompressibility. The remanent flux density of the doped elastomer was calculated to be 107 mT which reconciles with comparable works in [17] and [21].

B. The Multi-Segment Tentacle

As with the single segment arrangement the multi-segment tentacle was hung in the vertically aligned homogeneous field of the Helmholtz coil. For the multi-segment model, a field of 5mT was applied (10mT actuating fields appear in the supporting video). Images of the tentacles were taken on the same camera as the single segment arrangement and again processed in GIMP 2.10. After superimposition of the undeformed and deformed images from the experimental setup, deflections were measured along the x-axis from centre to centre of each of the three magnetized segments. Due to the rigid tubular formwork used during the fabrication process, unactuated tentacle deformations are minimal (MAPE 0.27mm or 0.6% of robot length, when subject to gravity). Furthermore, the zero line for deflection measurements is taken from the unactuated tentacle position, thus mitigating the worst of any residual unactuated deformation.

VII. Results

The analytical result derived in Section III using (3) is shown in Fig. 8 and can be seen to produce a less than accurate

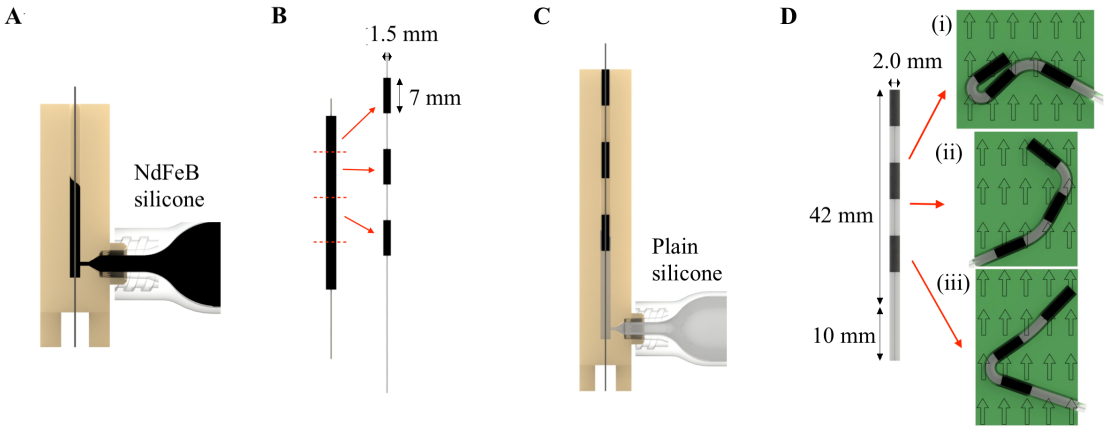

Figure 6. . Fabrication process of a multi-segment tentacle. (A) Injection molding of a continuous, magnetizable tentacle of diameter 1.5mm. (B) Once cured, the elastomer is cut into 7mm segments and positioned along the Nitinol needle at 14mm centres. (C) The needle is placed in a second mold of diameter 2mm and injected with plain silicone. (D) After curing, demolding and needle removal, the tentacle is placed in a 3D printed magnetizing tray. Here the three trays (i), (ii) and (iii) correspond to the scenarios A, B and C shown in Section VII Results.

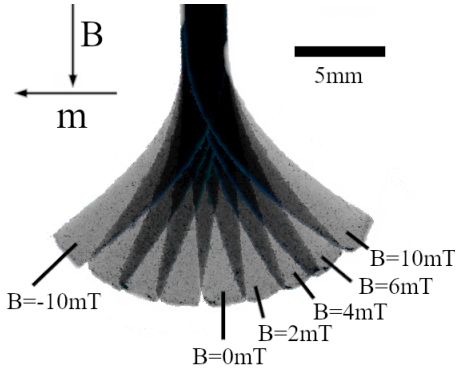

Figure 7. Superimposition of experimental results for fixed magnetization'm' for the range of Magnetic fluxes from B=-10mT to B=10mT in 2mT increments. For the purposes of visual clarity some results are omitted. The upper 10mm of the elastomer is restrained on a Nitinol pin whilst the lower 10mm is free to deform. A video of this actuation is included in the supplementary material.

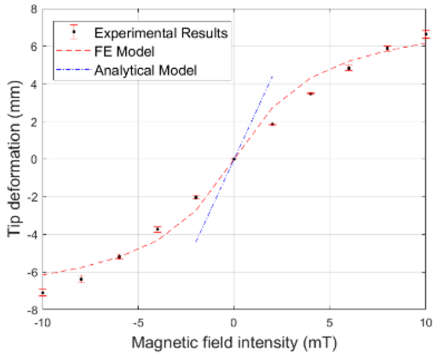

Figure 8. A comparison of deformations for Experimental, Numerical and Analytical solutions for the homogeneously magnetized single segment elastomer. The average error between experimental and numerical output is 14.9%. As can be observed, the linear beam analytical model offers a fairly poor approximation for this highly non-linear system, particularly at higher strains.

replica of experimental and numerical results even in the small strain region. As deflection increases the linear analytical model becomes increasingly inaccurate, quickly reaching a point where it can no longer be said to represent the behavior of the tentacle at all.

The single-segment FEM results, also shown in Fig. 8, reflect the experimental results with a MAPE of 14.9% up to the maximum field strengths of ±10mT. This result effectively verifies the material and magnetic properties of the elastomer in the numerical model and provides the requisite confidence in the FEM to extend the simulation up to the multi-segment tentacle.

As shown in Fig. 9, the multi-segment system was tested using three different x-axis desired deflections. The trained ANN translated these idealized outcomes into magnetization vectors based on its learnt weights. These magnetization vectors were input into the original FEM for validation. For the three candidate profiles the ANN replicated the FEM with a MAPE of 4.4%. This reconciles with the validation error of 6.3% shown in Section IV-B.

Table I shows absolute x-axis deflection and, in brackets, x-axis deflection as a percentage of maximum. The absolute deflection reveals discrepancies in magnitude between experimental and numerical results. From the images in Fig. 9, it can be observed that the experimental prototypes are deforming into a comparable *shape* to those requested (if not by a comparable *magnitude*). As such, proportional deflections are included to give a comparison of shape only. This normalizing process has been included purely for representational reasons; to enable the visual shape comparison available in Fig. 9 to be quantified. The existence of this adjustment is a recognition of two key limitations of this study. The first relates to the un-modelled three-dimensional effects unavoidably embedded in the multi-segment experiment. To accurately replicate the two-dimensional assumption made in the numerical model we would need to magnetize our specimens in a perfectly planar and twist-free fashion. This is unachievable and the consequence of any unwanted axial rotation introduced here is a loss of magnetic moment in the plane being considered. The second limitation is the non-automated fabrication and magnetization process of the multi-segment arrangement. As discussed earlier, the tentacle does not exactly achieve its intended dimensions, exhibits some unactuated deformation and, additionally, will not be magnetized in exactly the intended directions.

Both of these factors are significant areas for future work discussed in Section VIII. Furthermore errors may well persist in the measurement and calculation of material and magnetic properties. Notwithstanding this, after normalization, the *shape* profiles give results with a MAPE across all scenarios of 7.8%, calculated as

$$\epsilon = \frac{\sum_{j=1}^{3}\sum_{i=1}^{3}(|\delta x_{i,j}^{exp(norm)} - \delta x_{i,j}^{requested}|)}{\sum_{j=1}^{3}\sum_{i=1}^{3}(|\delta x_{i,j}^{requested}|)}$$

Where i = segment number, j = scenario number and $\delta x_{i,j}^{exp(norm)}$ = normalized experimentally measured deflection, calculated as

$$\delta x_{i,j}^{exp(norm)} = \delta x_{i,j}^{exp} . \frac{\sum_{i=1}^{3}(|\delta x_{i,j}^{requested}|)}{\sum_{i=1}^{3}(|\delta x_{i,j}^{exp}|)}$$

Table I
A COMPARISON OF X-AXIS DEFLECTION FOR THE INPUT TO THE NEURAL NETWORK, THE OUTPUT OF THE FEM AND THE EXPERIMENTAL READINGS. DEFLECTIONS ARE ALSO SHOWN, IN BRACKETS, AS PERCENTAGE OF MAXIMUM.

Scenario A

Segment Number	*Requested x Deflection (mm)*	*Numerical Deflection (mm)*	*Experimental Deflection (mm)*
1	2 (33%)	2.1 (33%)	0.9 (35%)
2	6 (100%)	6.4 (100%)	2.6 (100%)
3	5 (83%)	5.4 (84%)	2.2 (85%)

Scenario B

Segment Number	*Requested x Deflection (mm)*	*Numerical Deflection (mm)*	*Experimental Deflection (mm)*
1	-1 (50%)	-1.0 (53%)	-0.4 (44%)
2	-2 (100%)	-1.9 (100%)	-0.9 (100%)
3	1 (-50%)	1.1 (-58%)	0.4 (-44%)

Scenario C

Segment Number	*Requested x Deflection (mm)*	*Numerical Deflection (mm)*	*Experimental Deflection (mm)*
1	1 (-20%)	1 (-21%)	0.4 (-12%)
2	0 (0%)	0.1 (-2%)	-0.5 (15%)
3	-5 (100%)	-4.8 (100%)	-3.3 (100%)

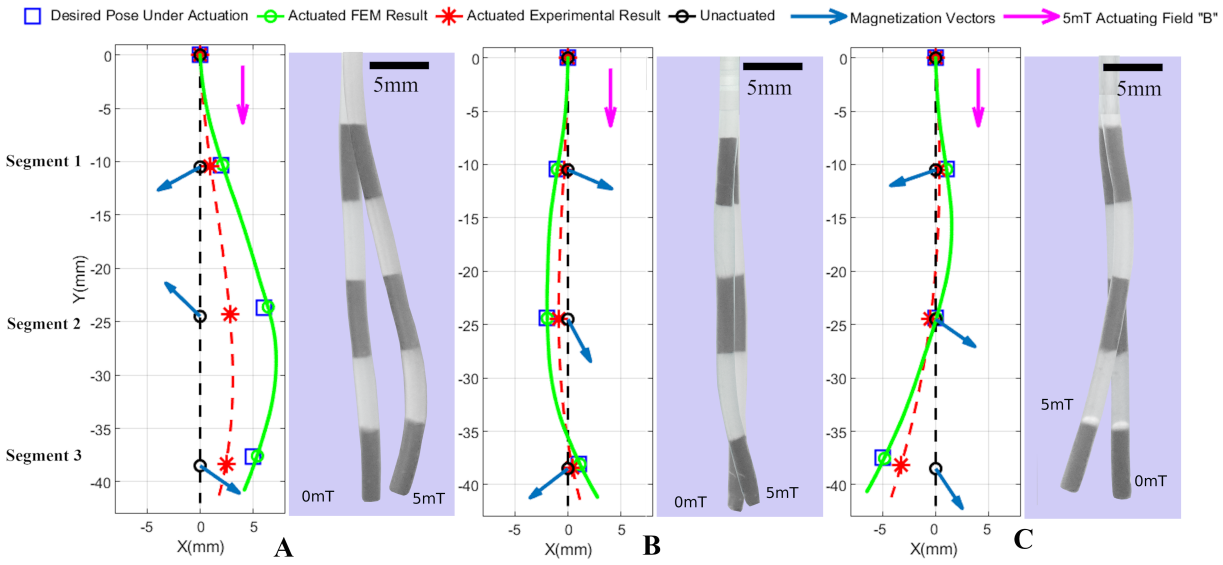

Figure 9. Sample experimental results shown against numerical results for three predefined scenarios of the full tentacle. The magnetization vectors are the output of the trained Neural Network using desired deflections as input. The experimental result on the right is shown with B=0 and 5mT. The graphical result on the left shows both experimental and numerical outcomes. (A) Desired deflections (top to bottom) of δx = [2 6 5] (mm). (B) δx = [-1 -2 1] (mm). (C) δx = [1 0 -5] (mm).

Where $\delta x_{i,j}^{exp}$ = experimentally measured deflection and $\delta x_{i,j}^{requested}$ = requested deflection from initial desired path.

More work will of course be required to understand the discrepancy observed in the magnitude of deflection.

VIII. Conclusions

Once trained, the ANN produces a reliable replica of the FEM and is capable of producing forward and inverse static results in real-time with 6.1% MAPE. This system of design, of course, is not limited to magnetically actuated CMs and could well be generalized to other applications. Once duplicate results have been removed from the training data (Section IV-A), the ANN can provide a useful surrogate of the numerical model subject to one further caveat; the operational workspace of the robot. Without external assistance the ANN, unlike the FEM, has no indication of which deformations lie within or outside of the physical scope of the system. This requires additional restrictions to the neural network, connecting desired deflections to the lookup table of possible outcomes. At present these restrictions are applied on a manually observed basis but for future work this system should be automated.

Beyond the accuracy of the learner, any significant further errors can be attributed to the modelling assumptions entering the FEM and to limitations in the manual fabrication and magnetization process. These will be reduced with further experimentation, fabrication process refinement, the inclusion of more sophisticated elasticity and magnetic field models in the FEM and inclusion of the third spatial dimension. In any future application of the proposed method, we would also aim to integrate an appropriate sensing technique (e.g. [30], [31], [32], [33]) to identify and balance the discrepancy between model and reality. This could inform a specific magnetic field controller which, in turn, would adjust the field to achieve the desired shape.

As well as the above improvements this work can now be extended for more convoluted, real-world trajectories derived from pre-operative imaging. This will be enabled by a greater variety of input variables (including geometric) to the lookup table. In addition to this, stiffening under actuating fields is known to occur for magnetic elastomers [34], harnessing this property to improve the capabilities of magnetic tentacles will form an interesting area of future research. It should also be noted that the current technique for generating magnetic fields is limited to homogeneous field generation within a centimetre scale workspace and therefore unsuitable for clinical application. For future feasibility, and also to address the issue of dynamic shape forming for navigation, there are a variety of potential methods of field generation available which operate on a much larger scale and with higher degrees of freedom [35], [36], [10]. In particular [12] and [37] propose magnetic manipulation using a permanent magnet positioned at the end effector of a medical-grade serial robotic manipulator whilst [13] employ an electromagnetic actuator hosted on a similar serial robot arm providing a clinically relevant workspace. Furthermore [38] propose actuation by means of a clinically-relevant external magnetic resonance imaging (MRI) system.

Looking further ahead, with improved sensing technology, we may be able to eliminate the FE model altogether and train the ANN from incoming sensory data thus fully eliminating modelling error and further harnessing the enormous potential of Machine Learning. With this work we have begun to demonstrate the potential of our magnetic shape forming tentacles and their scope to, in future works, conform to specific anatomical constraints.

References

[1] G. S. Litynski, "Laparoscopy–the early attempts: spotlighting Georg Kelling and Hans Christian Jacobaeus," *JSLS : Journal of the Society of Laparoendoscopic Surgeons*, vol. 1, no. 1, pp. 83–85, 1997. [Online]. Available: https://www.ncbi.nlm.nih.gov/pubmed/9876654https://www.ncbi.nlm.nih.gov/pmc/articles/PMC3015224/

[2] K. A. Hausegger, P. Schedlbauer, H. A. Deutschmann, and K. Tiesenhausen, "Complications in endoluminal repair of abdominal aortic aneurysms," *European journal of radiology*, vol. 39, no. 1, pp. 22–33, 2001.

[3] J. Burgner-Kahrs, D. C. Rucker, and H. Choset, "Continuum robots for medical applications: A survey," *IEEE Transactions on Robotics*, vol. 31, no. 6, pp. 1261–1280, 2015.

[4] I. De Falco, M. Cianchetti, and A. Menciassi, "A soft multi-module manipulator with variable stiffness for minimally invasive surgery," *Bioinspiration & Biomimetics*, vol. 12, no. 5, p. 56008, 2017. [Online]. Available: http://dx.doi.org/10.1088/1748-3190/aa7ccd

[5] C. Heunis, J. Sikorski, and S. Misra, "Flexible Instruments for Endovascular Interventions: Improved Magnetic Steering, Actuation, and Image-Guided Surgical Instruments," *IEEE Robotics and Automation Magazine*, vol. 25, no. 3, pp. 71–82, 2018.

[6] Y. Kim, S. S. Cheng, M. Diakite, R. P. Gullapalli, J. M. Simard, and J. P. Desai, "Toward the development of a flexible mesoscale mri-compatible neurosurgical continuum robot," *IEEE Transactions on Robotics*, vol. 33, no. 6, pp. 1386–1397, Dec 2017.

[7] A. Benouhiba, K. Rabenorosoa, P. Rougeot, M. Ouisse, and N. Andreff, "A multisegment electro-active polymer based milli-continuum soft robots," in *2018 IEEE/RSJ International Conference on Intelligent Robots and Systems (IROS)*. IEEE, 2018, pp. 7500–7506.

[8] S. Jeon, A. K. Hoshiar, K. Kim, S. Lee, E. Kim, S. Lee, J.-y. Kim, B. J. Nelson, H.-J. Cha, B.-J. Yi, and H. Choi, "A Magnetically Controlled Soft Microrobot Steering a Guidewire in a Three-Dimensional Phantom Vascular Network," *Soft Robotics*, vol. 6, no. 1, pp. 54–68, oct 2018. [Online]. Available: https://doi.org/10.1089/soro.2018.0019

[9] J. Martin, J. Martin, J. Norton, K. L. Obstein, and P. Valdastri, "Toward Autonomous Robotic Colonoscopy: Motion Strategies for Magnetic Capsule Navigation," in *2018 IEEE International Conference on Cyborg and Bionic Systems (CBS)*, 2018, pp. 240–244.

[10] J. Edelmann, A. J. Petruska, and B. J. Nelson, "Magnetic control of continuum devices," *The International Journal of Robotics Research*, vol. 36, no. 1, pp. 68–85, 2017. [Online]. Available: https://doi.org/10.1177/0278364916683443

[11] L. Barducci, G. Pittiglio, J. C. Norton, K. L. Obstein, and P. Valdastri, "Adaptive dynamic control for magnetically actuated medical robots," *IEEE robotics and automation letters*, vol. 4, no. 4, pp. 3633–3640, 2019.

[12] J. C. Norton, P. R. Slawinski, H. S. Lay, J. W. Martin, B. F. Cox, G. Cummins, M. P. Desmulliez, R. E. Clutton, K. L. Obstein, S. Cochran, and P. Valdastri, "Intelligent magnetic manipulation for gastrointestinal ultrasound," *Science Robotics*, vol. 4, no. 31, pp. 1–14, 2019.

[13] C. M. Heunis, Y. P. Wotte, J. Sikorski, G. P. Furtado, and S. Misra, "The armm system-autonomous steering of magnetically-actuated catheters: Towards endovascular applications," *IEEE Robotics and automation letters*, vol. 5, no. 2, pp. 704–711, 2020.

[14] Y. Kim, G. A. Parada, S. Liu, and X. Zhao, "Ferromagnetic soft continuum robots," *Science Robotics*, vol. 4, no. 33, p. eaax7329, 2019.

[15] Y. Kim, H. Yuk, R. Zhao, S. A. Chester, and X. Zhao, "Printing ferromagnetic domains for untethered fast-transforming soft materials," *Nature*, vol. 558, no. 7709, p. 274, 2018.

[16] T. Xu, J. Zhang, M. Salehizadeh, O. Onaizah, and E. Diller, "Millimeter-scale flexible robots with programmable three-dimensional magnetization and motions," *Science Robotics*, vol. 4, no. 29, p. eaav4494, 2019.

[17] G. Z. Lum, Z. Ye, X. Dong, H. Marvi, O. Erin, W. Hu, and M. Sitti, "Shape-programmable magnetic soft matter," *Proceedings of the National Academy of Sciences*, vol. 113, no. 41, pp. E6007 LP – E6015, oct 2016. [Online]. Available: http://www.pnas.org/content/113/41/E6007.abstract

[18] D. C. Rucker and R. J. Webster, "Statics and dynamics of continuum robots with general tendon routing and external loading," *IEEE Transactions on Robotics*, 2011.

[19] R. J. Webster and B. A. Jones, "Design and Kinematic Modeling of Constant Curvature Continuum Robots: A Review," *The International Journal of Robotics Research*, vol. 29, no. 13, pp. 1661–1683, jun 2010. [Online]. Available: https://doi.org/10.1177/0278364910368147

[20] R. J. Roesthuis and S. Misra, "Steering of Multisegment Continuum Manipulators Using Rigid-Link Modeling and FBG-Based Shape Sensing," *IEEE Transactions on Robotics*, vol. 32, no. 2, pp. 372–382, 2016.

[21] R. Zhao, Y. Kim, S. A. Chester, P. Sharma, and X. Zhao, "Mechanics of hard-magnetic soft materials," *Journal of the Mechanics and Physics of Solids*, vol. 124, pp. 244–263, 2019. [Online]. Available: http://www.sciencedirect.com/science/article/pii/S0022509618307646

[22] V. Q. Nguyen, A. S. Ahmed, and R. V. Ramanujan, "Morphing soft magnetic composites," *Advanced Materials*, vol. 24, no. 30, pp. 4041–4054, 2012.

[23] W. Hu, G. Z. Lum, M. Mastrangeli, and M. Sitti, "Small-scale soft-bodied robot with multimodal locomotion," *Nature*, vol. 554, no. 7690, p. 81, 2018.

[24] I. A. Seleem, H. El-Hussieny, and S. F. M. Assal, "Motion Planning for Continuum Robots: A Learning from Demonstration Approach," in *2018 27th IEEE International Symposium on Robot and Human Interactive Communication (RO-MAN)*, 2018, pp. 868–873.

[25] M. T. Gillespie, C. M. Best, E. C. Townsend, D. Wingate, and M. D. Killpack, "Learning nonlinear dynamic models of soft robots for model predictive control with neural networks," in *2018 IEEE International Conference on Soft Robotics (RoboSoft)*, 2018, pp. 39–45.

[26] M. Pfeiffer, C. Riediger, J. Weitz, and S. Speidel, "Learning soft tissue behavior of organs for surgical navigation with convolutional neural networks," *International Journal of Computer Assisted Radiology and Surgery*, vol. 14, no. 7, pp. 1147–1155, 2019. [Online]. Available: https://doi.org/10.1007/s11548-019-01965-7

[27] A. Madani, A. Bakhaty, J. Kim, Y. Mubarak, and M. R. K. Mofrad, "Bridging Finite Element and Machine Learning Modeling: Stress Prediction of Arterial Walls in Atherosclerosis," *Journal of Biomechanical Engineering*, vol. 141, no. 8, may 2019. [Online]. Available: https://doi.org/10.1115/1.4043290

[28] S. Nair, *Introduction to continuum mechanics*. Cambridge University Press, 2009.

[29] S. Jeon, A. K. Hoshiar, S. Kim, S. Lee, E. Kim, S. Lee, K. Kim, J. Lee, J.-y. Kim, and H. Choi, "Improving guidewire-mediated steerability of a magnetically actuated flexible microrobot," *Micro and Nano Systems Letters*, vol. 6, no. 1, p. 15, 2018. [Online]. Available: https://doi.org/10.1186/s40486-018-0077-y

[30] A. Z. Taddese, P. R. Slawinski, M. Pirotta, E. De Momi, K. L. Obstein, and P. Valdastri, "Enhanced real-time pose estimation for closed-loop robotic manipulation of magnetically actuated capsule endoscopes," *The International journal of robotics research*, vol. 37, no. 8, pp. 890–911, 2018.

[31] D. Son, S. Yim, and M. Sitti, "A 5-d localization method for a magnetically manipulated untethered robot using a 2-d array of hall-effect sensors," *IEEE/ASME Transactions on Mechatronics*, vol. 21, no. 2, pp. 708–716, 2015.

[32] F. Khan, A. Denasi, D. Barrera, J. Madrigal, S. Sales, and S. Misra, "Multi-core optical fibers with bragg gratings as shape sensor for flexible medical instruments," *IEEE sensors journal*, 2019.

[33] G. J. Vrooijink, M. Abayazid, and S. Misra, "Real-time three-dimensional flexible needle tracking using two-dimensional ultrasound," in *2013 IEEE International Conference on Robotics and Automation*. IEEE, 2013, pp. 1688–1693.

[34] Y. Li, J. Li, W. Li, and H. Du, "A state-of-the-art review on magnetorheological elastomer devices," *Smart materials and structures*, vol. 23, no. 12, p. 123001, 2014.

[35] L. B. Kratchman, T. L. Bruns, J. J. Abbott, and R. J. Webster, "Guiding elastic rods with a robot-manipulated magnet for medical applications," *IEEE Transactions on Robotics*, vol. 33, no. 1, pp. 227–233, Feb 2017.

[36] K. M. Popek, T. Hermans, and J. J. Abbott, "First demonstration of simultaneous localization and propulsion of a magnetic capsule in a lumen using a single rotating magnet," in *2017 IEEE International Conference on Robotics and Automation (ICRA)*, May 2017, pp. 1154–1160.

[37] P. R. Slawinski, A. Z. Taddese, K. B. Musto, K. L. Obstein, and P. Valdastri, "Autonomous retroflexion of a magnetic flexible endoscope," *IEEE Robotics and Automation Letters*, vol. 2, no. 3, pp. 1352–1359, July 2017.

[38] A. Azizi, C. C. Tremblay, K. Gagné, and S. Martel, "Using the fringe field of a clinical mri scanner enables robotic navigation of tethered instruments in deeper vascular regions," *Science Robotics*, vol. 4, no. 36, 2019.